GAMM-Mitt. **38**, No. 2, 213 – 227 (2015) / **DOI** 10.1002/gamm.201510012

Linking atomistic, kinetic Monte Carlo and crystal plasticity simulations of single-crystal tungsten strength

David Cereceda[1,2,3,*], **Martin Diehl**[4], **Franz Roters**[4], **Pratheek Shanthraj**[4,5], **Dierk Raabe**[4], **José Manuel Perlado**[2], and **Jaime Marian**[1,3]

[1] Materials Science and Engineering Department, University of California, Los Angeles, California 90095-1597

[2] Instituto de Fusión Nuclear, Universidad Politécnica de Madrid, E-28006 Madrid, Spain

[3] Physical and Life Sciences Directorate, Lawrence Livermore National Laboratory, Livermore, CA, USA

[4] Max-Planck-Institut für Eisenforschung, Max-Planck-Straße 1, 40237 Düsseldorf, Germany

[5] Aachen Institute for Advanced Study in Computational Engineering Science, RWTH Aachen University, Schinkelstraße 2, D-52062 Aachen, Germany

Received 6 March 2015, revised 26 June 2015, accepted 6 July 2015
Published online 3 September 2015

Key words Crystal plasticity, multiscale, single crystal, non-Schmid, screw dislocation, slip, bcc, tungsten, uniaxial

Understanding and improving the mechanical properties of tungsten is a critical task for the materials fusion energy program. The plastic behavior in body-centered cubic (bcc) metals like tungsten is governed primarily by screw dislocations on the atomic scale and by ensembles and interactions of dislocations at larger scales. Modeling this behavior requires the application of methods capable of resolving each relevant scale. At the small scale, atomistic methods are used to study single dislocation properties, while at the coarse-scale, continuum models are used to cover the interactions between dislocations. In this work we present a multiscale model that comprises atomistic, kinetic Monte Carlo (kMC) and continuum-level crystal plasticity (CP) calculations. The function relating dislocation velocity to applied stress and temperature is obtained from the kMC model and it is used as the main source of constitutive information into a dislocation-based CP framework. The complete model is used to perform material point simulations of single-crystal tungsten strength. We explore the entire crystallographic orientation space of the standard triangle. Non-Schmid effects are inlcuded in the model by considering the twinning-antitwinning (T/AT) asymmetry in the kMC calculations. We consider the importance of $\langle 1\,1\,1\rangle\{1\,1\,0\}$ and $\langle 1\,1\,1\rangle\{1\,1\,2\}$ slip systems in the homologous temperature range from $0.08T_m$ to $0.33T_m$, where T_m=3680 K is the melting point in tungsten.

* Corresponding author E-mail: davidcereceda@ucla.edu

1 Introduction

Tungsten and tungsten alloys are being considered as leading candidates for structural and functional materials in future fusion energy devices. The most attractive properties of tungsten for the design of magnetic fusion energy reactors are its high melting point and thermal conductivity, low sputtering yield and low long-term disposal radioactive footprint. However, tungsten also presents a very low fracture toughness, mostly associated with inter-granular failure and bulk plasticity, that limits its applications [1–3].

The plastic behavior of bcc refractory metals like tungsten is governed by the kink-pair mediated thermally activated motion of $\frac{1}{2}\ \langle 1\,1\,1\rangle$ screw dislocations [4–7]. Dislocation slip in bcc metals has been reported in the literature on $\{1\,1\,0\}$, $\{1\,1\,2\}$ and $\{1\,2\,3\}$ slip planes. While some authors have suggested that the temperature range determines the activation of slip planes ($\{1\,1\,0\}$ and $\{1\,1\,2\}$ planes at lower temperatures, $\{1\,2\,3\}$ planes at higher temperatures) [8–10] , other works propose the decomposition of slip into $\{1\,1\,2\}$ and $\{1\,2\,3\}$ planes on alternating $\{1\,1\,0\}$ planes, suggesting that slip occurs only on $\{1\,1\,0\}$ slip planes at room temperature [11–15]. Schmid's law, which is used to determine the active slip planes for a specific stress state [16] is known to break down for bcc metals. This particularity with a big impact on the plastic flow is referred to as *non-Schmid behavior*, and it implies that the critical resolved shear stress defining the onset of dislocation glide on a given slip plane varies with the sign of the applied stress and the orientation of the loading axis with respect to the lattice [17, 18].

A whole variety of crystal plasticity (CP) constitutive models have been proposed and discussed in the literature to solve multiple plasticity problems in materials. There are two main groups of constitutive models differentiated by the nature of the state variable they use: phenomenological models mostly use a critical resolved shear stress as state variable for each slip system [19–22], while physically-based constitutive models rely on the dislocation density as state variable since dislocations are considered the main carriers of plasticity [23–25]. Most of the existing CP frameworks have been focused on fcc metals [26–29], while only a few studies have been devoted to study bcc plasticity. The selection of active slip systems in the constitutive framework will also affect the predictions of the model. The incorporation of non-Schmid effects can be used as a differentiating feature among the models for bcc materials. Table 1 presents the most important examples of CP models for bcc metals classified by the previous criteria.

In this work, we present a CP framework to obtain the yield strength in single-crystal tungsten. The constitutive model is built on physically-based mobility functions [1] for $\frac{1}{2}$ $\langle 1\,1\,1\rangle$ screw dislocations obtained via kMC simulations, which include the characteristic *non-Schmid* behavior of bcc metals. Another important aspect in our simulations is the consideration of the entire family of $\{1\,1\,0\}\langle 1\,1\,1\rangle$ and $\{1\,1\,2\}\langle 1\,1\,1\rangle$ slip systems (twelve each) and combinations thereof. We simulate uniaxial tensile tests along 231 different crystallographic orientations in the standard triangle. The temperature range covered goes from room temperature to $\frac{1}{3}\ T_m$, where T_m=3680 K is the melting point for tungsten [51]. The orientation dependence of the stress-strain curves and the temperature dependence of the yield stress predicted by our model are in qualitative agreement with previous results in other bcc metals [52–54].

[1] The mobility function represents the relation between the dislocation velocity and the state variables stress and temperature.

Table 1 CP constitutive models for bcc metals.

	Slip planes		
	$\{1\,1\,0\}$	$\{1\,1\,0\}, \{1\,1\,2\}$	$\{1\,1\,0\}, \{1\,1\,2\}, \{1\,2\,3\}$
Schmid	Peeters *et al.* (2000) [30] Stainier *et al.* (2002) [31]	Raphael *et al.* (1985) [32] [33] Kitayama *et al.* (2013) [34]	Holscher *et al.* (1991,1994) [35,36] Raabe *et al.* (1994,1995) [8,37,38] Ma *et al.* (2006) [9] Hamelin *et al.* (2011) [39]
non-Schmid	Koester *et al.* (2012) [40] Weinberger *et al.* (2012) [41] Narayanan *et al.* (2013) [42] Patra *et al.* (2014) [43] Lim *et al.* (2015) [44,45]	Lee *et al.* (1999) [46] Kuchinicki *et al.* (2008) [47] Lim *et al.* (2013) [48] Alankar *et al.* (2013) [49] Knezevic *et al.* (2014) [50]	-

The paper is organized as follows. The formulation of the constitutive model proposed is described in Section 2. Simulation details and the predictor-corrector scheme are presented in Section 3. In Section 4 we report the CP calculations in single-crystal tungsten as a function of the Schmid behavior, glide plane, loading direction and temperature. Final concluding remarks are given in Section 5.

2 Constitutive model

We use the multiplicative decomposition of the deformation gradient $\mathbf{F}$:

$$\mathbf{F} = \mathbf{F}_e\mathbf{F}_p \tag{1}$$

where $\mathbf{F}_e$ and $\mathbf{F}_p$ are the elastic and plastic deformation gradients, respectively [55]. The plastic deformation evolves as:

$$\dot{\mathbf{F}}_p = \mathbf{L}_p\mathbf{F}_p \tag{2}$$

where $\mathbf{L}_p$ is the deformation velocity gradient. In the case of dislocation slip as the only deformation process (no mechanical twinning or martensitic transformations considered), $\mathbf{L}_p$ can be formulated as:

$$\mathbf{L}_p = \sum_\alpha \dot{\gamma}^\alpha \mathbf{M}^\alpha = \sum_\alpha \dot{\gamma}^\alpha \mathbf{m}^\alpha \otimes \mathbf{n}^\alpha \tag{3}$$

Here, the running index α goes from 1 to n, where n is the total number of slip systems; $\mathbf{m}^\alpha$ and $\mathbf{n}^\alpha$ are unit vectors representing the normalized slip direction and the normal to the slip plane of the system α, respectively; $\dot{\gamma}^\alpha$ is the shear rate on system α, given by the Orowan equation:

$$\dot{\gamma}^\alpha = \rho^\alpha b v^\alpha \tag{4}$$

where b is the magnitude of the Burgers vector, ρ^α is the density of mobile dislocations and v^α is the dislocation velocity on slip system α.

2.1 Dislocation velocity function

In bcc metals such as tungsten, screw dislocations with Burgers vector $\mathbf{b} = \frac{1}{2}\,[1\,1\,1]$ are the main carriers of plastic shear due to their low mobility, which is a cosequence of their non-planar core structure [56–58]. At low temperatures, screw motion proceeds via thermally activated nucleation and subsequent lateral propagation of kink pairs. By contrast, edge dislocations display viscous motion (linear with the applied stress) and thus screw motion is the rate-limiting step for plastic shear. Molecular dynamics (MD) is commonly used to simulate dislocation motion [59–61], although it is generally not suited to capture rare-event mechanisms (such as nucleation). In bcc crystals, MD simulations naturally include non-Schmid effects as part of the simulated dynamics of screw dislocation motion, but they provide overdriven dynamics and are limited to glide on $\{1\,1\,2\}$ planes due to limitations with boundary conditions and said non-Schmid effects [60,61]. An alternative technique that is not subjected to this limitation is kMC [62–64]. Therefore we choose a mobility function extracted from the kMC simulations described by Stukowski *et al.* [64], where the twinning/anti-twinning asymmetry non-Schmid behavior has been captured.

Then, in the present model, $\{1\,1\,0\}\langle 1\,1\,1\rangle$ and $\{1\,1\,2\}\langle 1\,1\,1\rangle$ slip is described via screw dislocation mobility functions obtained beforehand using kMC simulations. The twinning/anti-twinning asymmetry is reflected in the fact that the dislocation velocity depends on the sign of the angle between the glide plane and the plane of maximum resolved shear stress. The dislocation mobility formulas capture this effect in an effective way, from data obtained during tens of different kMC runs. These laws provide the dependence of the velocity function on the stress and temperature:

$$\begin{aligned} v(s,T) &= A \cdot s^n \cdot f(s,T) \cdot [1 - B \cdot f(s,T)] \cdot \text{sign}(\tau^\alpha) \\ f(s,T) &= \exp\left\{ -\frac{\Delta H_0}{k_B T} \left(1 - s^p\right)^q \right\} \end{aligned} \tag{5}$$

where k_B is the Boltzmann constant; T is the absolute temperature; A, B, n, p, and q are all fitting parameters obtained from the kMC simulations and τ^α is the resolved shear stress.

Thus, non-Schmid effects are not an integral part of the CP formulation, but they enter the model via the above equations. Then, the resolved shear stress is defined as the geometric projection of the applied load on the slip system is considered. For small elastic strains, it reads as

$$\tau^{\alpha} = \boldsymbol{\sigma} : \mathbf{M}^{\alpha} \approx \mathbf{S} : \mathbf{M}^{\alpha}; \tag{6}$$

where $\mathbf{S}$ is the second Piola-Kirchhoff stress tensor, that can be expressed assuming hyperelasticity as a function of the elastic deformation gradient $\mathbf{F}_e$ and the stiffness tensor $\mathbb{C}$:

$$\mathbf{S} = \frac{\mathbb{C}}{2}(\mathbf{F}_e^T \mathbf{F}_e - \mathbf{I}) \tag{7}$$

We have chosen to work with a non dimensional scalar form of the stress tensor defined as

$$s = \frac{|\tau^{\alpha}| - \tau_{pass}}{\tau_p}, \tag{8}$$

where τ_p is the Peierls stress; τ_{pass} is the passing stress, defined as a function of the shear modulus μ, the local dislocation densities $\rho^{\alpha'}$, and the interaction parameters $\xi_{\alpha\alpha'}$ that characterize the interaction strength between slip systems α and α' as a result of the possible interaction types self, coplanar, collinear, mixed-asymmetrical junction (orthogonal), mixed-symmetrical junction (glissile) and edge junction (sessile) [65]:

$$\tau_{pass} = \mu b \sqrt{\sum_{\alpha'} \xi_{\alpha\alpha'} \rho^{\alpha'}}; \tag{9}$$

ΔH_0 is the activation enthalpy when s is equal to zero.

2.2 Dislocation density law

The evolution of the dislocation density on each slip system serves as an internal variable describing the current microstructural state. Different models that calculate the flow stress from dislocation densities have been discussed in the literature [23–28, 66, 67]. In this work we have used the model presented by Roters [68],

$$\dot{\rho}^{\alpha} = \dot{\rho}^{\alpha}_{\mathrm{mult}} + \dot{\rho}^{\alpha}_{\mathrm{ann}} \tag{10}$$

The evolution model is initialized by the dislocation density at $t = 0$, ρ_0^{α}. In eq. (10), $\dot{\rho}^{\alpha}_{\mathrm{mult}}$ and $\dot{\rho}^{\alpha}_{\mathrm{ann}}$ represent the dislocation multiplication and dislocation annihilation rate terms on slip system α, respectively. In this model, dislocation multiplication is treated as being proportional to the inverse mean free path of the dislocations, λ^{α}:

$$\dot{\rho}^{\alpha}_{\mathrm{mult}} = \frac{|\dot{\gamma}^{\alpha}|}{b\lambda^{\alpha}}, \tag{11}$$

defined as a function of the grain size d_{grain} and a hardening constant c,

$$\frac{1}{\lambda^\alpha} = \frac{1}{d_{grain}} + \frac{\sqrt{\rho^\alpha}}{c} \tag{12}$$

Dislocation annihilation occurs spontaneously when dipoles approach a spacing below d_{edge}:

$$\dot{\rho}^\alpha_{\mathrm{ann}} = -\frac{2d_{\mathrm{edge}}}{b}\rho^\alpha|\dot{\gamma}^\alpha| \tag{13}$$

3 Simulation details

The constitutive model described in Section 2 has been implemented in the the Düsseldorf Advanced Material Simulation Kit (DAMASK) [69]. This open source software allows the integration of the constitutive models within different solvers for mechanical equilibrium: a spectral method based solver and two commercial FEM solvers such as Abaqus and MSC.Marc. Based on its performance for single crystals, we have chosen the spectral method solution described in [70, 71] to perform tensile tests in single-crystal tungsten.

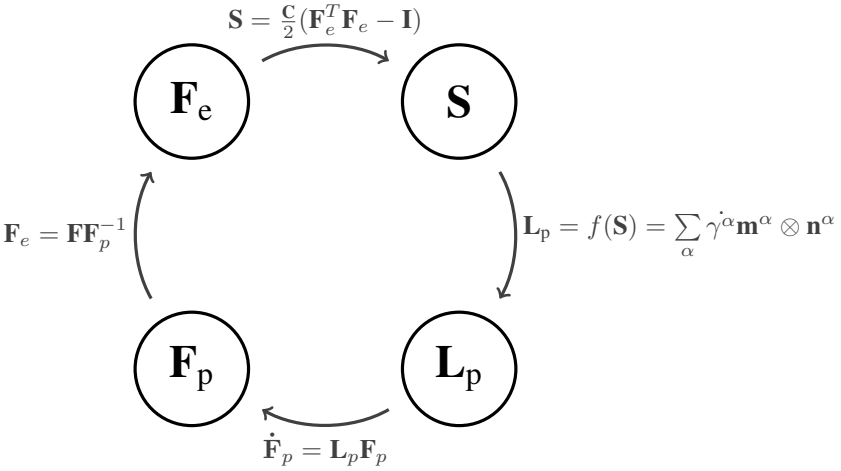

Fig. 1 Predictor-corrector scheme to calculate the stress **S** as a function of **F**.

The set of nonlinear equations (1), (2), (3) and (7), for which the dependency is summarized in Fig. 1, needs to be solved iteratively. In DAMASK, a Newton-Raphson scheme is used to do that and the velocity gradient $\mathbf{L}_\mathrm{p}$ is chosen as a predictor. Since $\mathbf{L}_\mathrm{p}$ is used as a predictor, the tangent $\frac{\delta \mathbf{L}_\mathrm{p}}{\delta \mathbf{S}}$ needs to be computed as well by the plasticity model. More details about the implementation are given in [72]. Choosing $\mathbf{L}_\mathrm{p}$ as initial step represents an advantage for the inversion of the Jacobi matrix during the Newton-Raphson algorithm, since the dimension of the Jacobi matrix is equal to the number of independent variables of the quantity that it is used as predictor, and these are its 9 components. However, when starting with $\mathbf{L}_\mathrm{p}$, slip rates $\dot{\gamma^\alpha}$ need to be calculated from the stress, which may generate important deviations as a consequence of the exponential nature of the shear rates [67, 69].

A schematic diagram of the multiscale procedure that links atomistic, kMC and CP simulations is shown in Fig. 2, where the relation between $\mathbf{L}_\mathrm{p}$ and the dislocation velocities v^α is achieved via Eq. 3. The core of the dislocation-based CP model is in the formulation of this Eq. 3. While some models include mechanical twinning and phase transformations, we have only considered dislocation glide as the main carrier of plastic deformation.

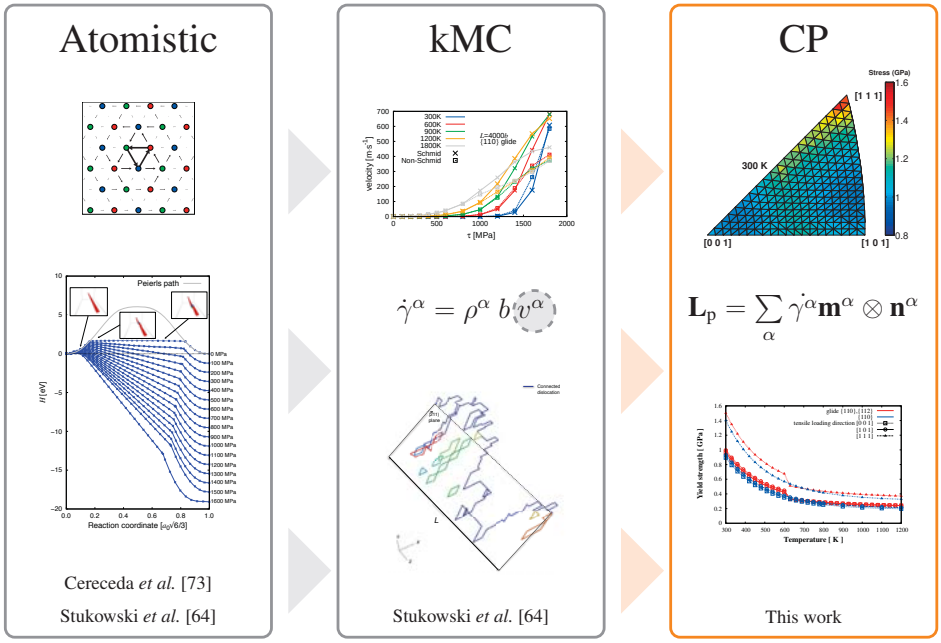

Fig. 2 (online colour at: www.gamm-mitteilungen.org) Schematic diagram of the multiscale approach that links atomistic, kinetic Monte Carlo and crystal plasticity simulations. In step I we use semiempirical interatomic potentials to calculate the energetics of single dislocation motion. In step II we use kMC parameterized with atomistic data to fit a mobility function to the velocity vs. stress vs. temperature. Finally, in step III, we use those mobility functions to characterize the velocity gradient in CP.

4 Results

In this section we perform uniaxial tensile tests in single-crystal tungsten under different crystallographic orientations in the standard triangle using the CP framework just described. We study the crystal response as a function of the number and type of slip planes, whether or not non-Schmid behavior is considered, and temperature.

The values of the parameters defined in the constitutive model are listed in tables 2 and 3. Most of the parameters of these tables have been obtained directly from kMC simulations [64] or first principle and atomistic calculations [73] with the EAM interatomic potential [74] used to parameterize the kMC model. For those parameters not derived from atomistic or kMC simulations (ρ_0^α, d_{grain}, c, d_{edge}, $\xi_{\alpha\alpha'}$) the values used merit some discussion. The initial dislocation density is defined as $\rho_0^\alpha \approx 1/L^2 \approx 10^{12}\mathrm{m}^{-2}$, with $L = 4000b$ the average dislocation segment length. The critical distance for dislocation annihilation is taken

Table 2 Fitting parameters of the mobility function defined in Eq. 5 (obtained from [64]).

	Schmid		**Non Schmid**		
	$\{1\,1\,0\}$ *glide*	$\{1\,1\,2\}$ *glide*	$\{1\,1\,0\}$ *glide*	$\{1\,1\,2\}$ *glide*	
				T $\leq$ 600 K	T $>$ 600 K
A	3693.4	755.59	1444.23	2084.19	3415.97
B	0.97	0.50	0.72	0.68	0.89
n	2.47	0.38	1.78	1.39	2.72
p	0.16	0.22	0.26	0.81	0.19
q	1.00	1.01	1.40	2.45	1.32

Table 3 List of parameters for the constitutive model. The last row represents the six coefficients of the interaction matrix.

Parameter	Value	Units		Parameter	Value	Units
k_B	8.617×10^{-5}	eV K^{-1}		τ_p	2.03	GPa
ΔH_0	1.63	eV		μ	161	GPa
a_0	3.143×10^{-10}	m		$\lvert\mathbf{b}\rvert$	2.72×10^{-10}	m
ρ_0^α	1.0×10^{12}	m^{-2}		d_{grain}	2.7×10^{-5}	m
c	10			d_{edge}	2.72×10^{-10}	m
$\xi_{\alpha\alpha'}$	0.009	0.009	0.72	0.05	0.09	0.06

from [51], where $d_{edge} = 2.7 \times 10^{-5}$ m. The hardening constat c and the grain size d_{grain} are set, respectively, to one and to an arbitrarily high value such that the term controlling the dislocation mean free path is: $\lambda^\alpha \approx (\sqrt{\rho^\alpha})^{-1}$. The interaction coefficients $\xi_{\alpha\alpha'}$ were computed for elastic isotropic iron [65], which make them suitable also for elastic isotropic tungsten. Since this work focuses on the yield stress and not on the entire stress-strain curve, the values assigned to these mentioned parameters that mainly influence the plastic regime of the model are considered a valid approximation.

4.1 Uniaxial tensile tests

The boundary conditions chosen to represent the uniaxial tensile tests along the z-direction are

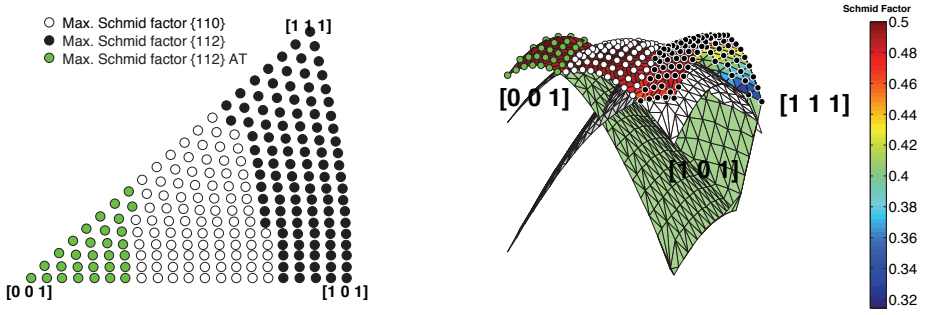

(a) (b)

Fig. 3 (online colour at: www.gamm-mitteilungen.org) Discretization of the standard triangle into a regular grid of 231 points representing different crystallographic orientations. 3(a) represents the the slip family with maximum Schmid factor. 3(b) shows the three dimensional surface of the Schmid factor. The envelope of maximum Schmid factor is colored coded according to Fig.3(a).

$$\frac{\dot{\mathbf{F}}}{10^{-3}s^{-1}} = \begin{bmatrix} * & * & * \\ 0 & * & * \\ 0 & 0 & \frac{d_z}{d_{z,0}} \end{bmatrix} \quad \text{and} \quad \frac{\mathbf{P}}{Pa} = \begin{bmatrix} 0 & 0 & 0 \\ * & 0 & 0 \\ * & * & * \end{bmatrix}, \tag{14}$$

with "*" denoting components for which complementary conditions are prescribed. These conditions are applied for 100 s in 300 equal increments resulting in a final z-tension of 0.1. Different loading orientations in the standard triangle are characterized by their Bunge Euler angles φ_1, ϕ and φ_2.

For a bcc slip system defined by slip direction $\mathbf{m}^\alpha$ and normal to the slip plane $\mathbf{n}^\alpha$, the Schmid factor for an applied tensile load along direction $\mathbf{l}$ can be calculated by

$$cos\Phi\ cos\lambda = \frac{\mathbf{l}\cdot\mathbf{m}^\alpha}{\parallel \mathbf{l} \parallel \cdot \parallel \mathbf{m}^\alpha \parallel} \cdot \frac{\mathbf{l}\cdot\mathbf{n}^\alpha}{\parallel \mathbf{l} \parallel \cdot \parallel \mathbf{n}^\alpha \parallel} \tag{15}$$

In this work, the Schmid factor has been computed for 231 crystallographic orientations uniformly distributed in the standard triangle. The maximum Schmid factor indicates the primary slip system for each loading direction. Fig. 3(a) shows three regions where the operational slip system corresponds to $\{1\,1\,0\}$, $\{1\,1\,2\}$ or $\{1\,1\,2\}$ anti-twinning (AT) families. These results from Fig.3(a) are in agreement with experimental work from Franciosi *et al.* [75]. The envelope of maximum Schmid factor plotted in Fig. 3(b) shows not only the operational slip family but also the value of the Schmid factors.

The resulting component of the *first Piola-Kirchoff stress* along loading direction is plotted in Fig. 4 as a function of the *Biot strain* $\mathbf{E}^{(1)} = \mathbf{U} - \mathbf{I} = (\lambda_i - 1)u_i \otimes u_i$, with λ_i and u_i being the eigenvalues and eigenvectors of the right stretch tensor $\mathbf{U} = \sqrt{\mathbf{F}^T\mathbf{F}}$. We have chosen to plot the *first Piola-Kirchoff stress* versus the *Biot strain* because they represent the engineering stress and engineering strain respectively.

The uniaxial loading directions shown in Fig. 4 are the three corners of the standard triangle: $[0\,0\,1]$, $[1\,0\,1]$, $[1\,1\,1]$. As it is expected for an isotropic material like tungsten, there is no orientation dependence on the *Young's modulus*, represented by the slope of the elastic regime [2]. On the other hand, there is an orientation dependence of the yield strength that matches observations from previous experiments and simulations in bcc metals [52, 76, 77].

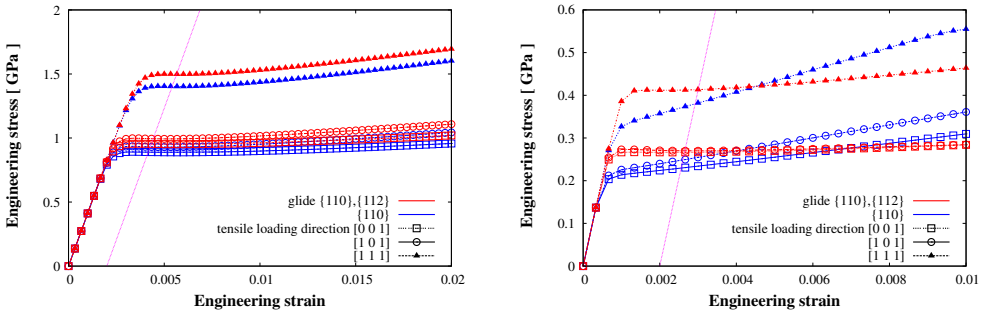

(a) Schmid, 300 K (b) non-Schmid, 900 K

Fig. 4 (online colour at: www.gamm-mitteilungen.org) Mechanical response of bcc W single-crystal predicted by our constitutive model under conditions of uniaxial tension along different loading directions and slip systems. The stress-strain behavior is represented using the components of the *first Piola-Kirchoff stress* and the *Biot strain* along the loading direction z. Parameters from Table 2 are taken for (a) Schmid behavior and (b) non-Schmid behavior.

The yield strength σ_y has been determined using the 0.2% strain offset method, where a straight line is constructed parallel to the elastic portion of the stress-strain curve for a strain offset of 0.002. The stress corresponding to the intersection of this line and the stress-strain curve as it bends over the plastic region is defined as the yield strength [78]. Figure 5 represents the yield strength as a function of the temperature for uniaxial tensile tests along the three corners of the standard triangle. As it is reported in previous works for bcc metals [52–54], yield strength decreases with temperature. Two different scenarios of slip have been considered in Fig. 4 and Fig. 5: (i) only the twelve $\{1\,1\,0\}\langle 1\,1\,1\rangle$ slip systems are active; (ii) $\{1\,1\,0\}\langle 1\,1\,1\rangle$ and $\{1\,1\,2\}\langle 1\,1\,1\rangle$ slip systems are active . We can see from Fig. 5 that the values of yield strength are higher if the non-Schmid effects are considered. Below 600 K, non-Schmid behavior also predicts slightly different results for the two scenarios of slip.

Figure 6 shows the loading directions corresponding to the five highest and lowest values of yield strength. Figure 7 shows the yield strength under uniaxial tension for 231 uniformly distributed loading directions within the standard stereographic triangle. The percentage difference between the yield strength with non-Schmid behavior, σ_y^{NS} (Fig. 7(b)), and the yield strength with Schmid behavior, σ_y^{S} (Fig. 7(a)), is defined as $\left|\frac{\sigma_y^{NS}-\sigma_y^{S}}{(\sigma_y^{NS}+\sigma_y^{S})/2}\right|$, and its value decreases with temperature (Fig. 7(c)). We can conclude from Fig. 6 and Fig. 7 that the maximum yield stength is always achieved when loading along $[1\,1\,1]$ while the loading direction of minimum yield strength depends on the temperature range and whether non-Schmid effects behavior are considered.

[2] The value of the Young's modulus for tungsten used in our simulations is 411 GPa [51].

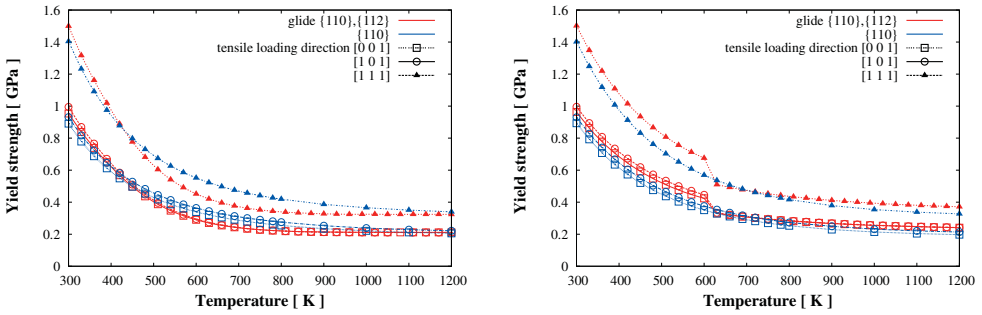

(a) Schmid (b) non-Schmid

Fig. 5 (online colour at: www.gamm-mitteilungen.org) Temperature dependence of yield strength for different tensile loading orientations and active slip systems. 5(a) represents Schmid behavior and 5(b) represents non-Schmid behavior.

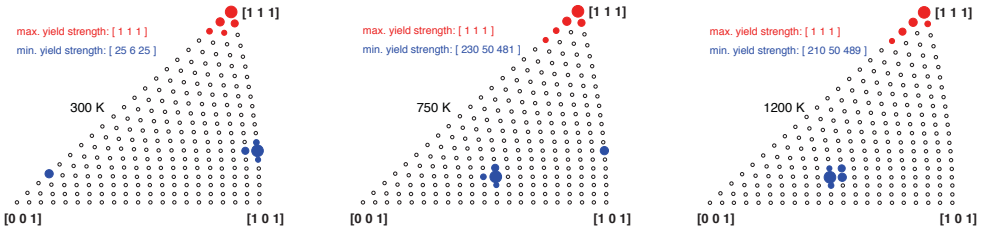

Fig. 6 (online colour at: www.gamm-mitteilungen.org) Loading directions corresponding to the five highest and lowest values of yield strength for uniaxial tensile tests at 300, 750 and 1200 K. The biggest blue circle represents the absolute minimum and the biggest red circle represents the absolute maximum.

5 Conclusions

To summarize, the main findings of this chapter can be condensed into the following aspects:

- We have performed single material point simulations in monocrystalline tungsten using a CP framework whose constitutive law is physically-based on the dislocation velocities obtained using a kMC model [64]. Most of the parameters required to formulate the CP framework are obtained using atomistic simulations and one EAM interatomic potential [74].

- We have incorporated in our model non-Schmid effects and compared their influence in the results with respect to the classic Schmid's law. The results shown in Fig. 5 and Fig. 7 reveal that adding the contribution of non-Schmid effects rises the values of yield strength. The difference between Schmid and non-Schmid behaviors also decreases when increasing the temperature.

- We have compared the results obtained when activating only $\{1\,1\,0\}\langle 1\,1\,1\rangle$ slip systems and a combination of both $\{1\,1\,0\}\langle 1\,1\,1\rangle$ and $\{1\,1\,2\}\langle 1\,1\,1\rangle$ slip systems. The results

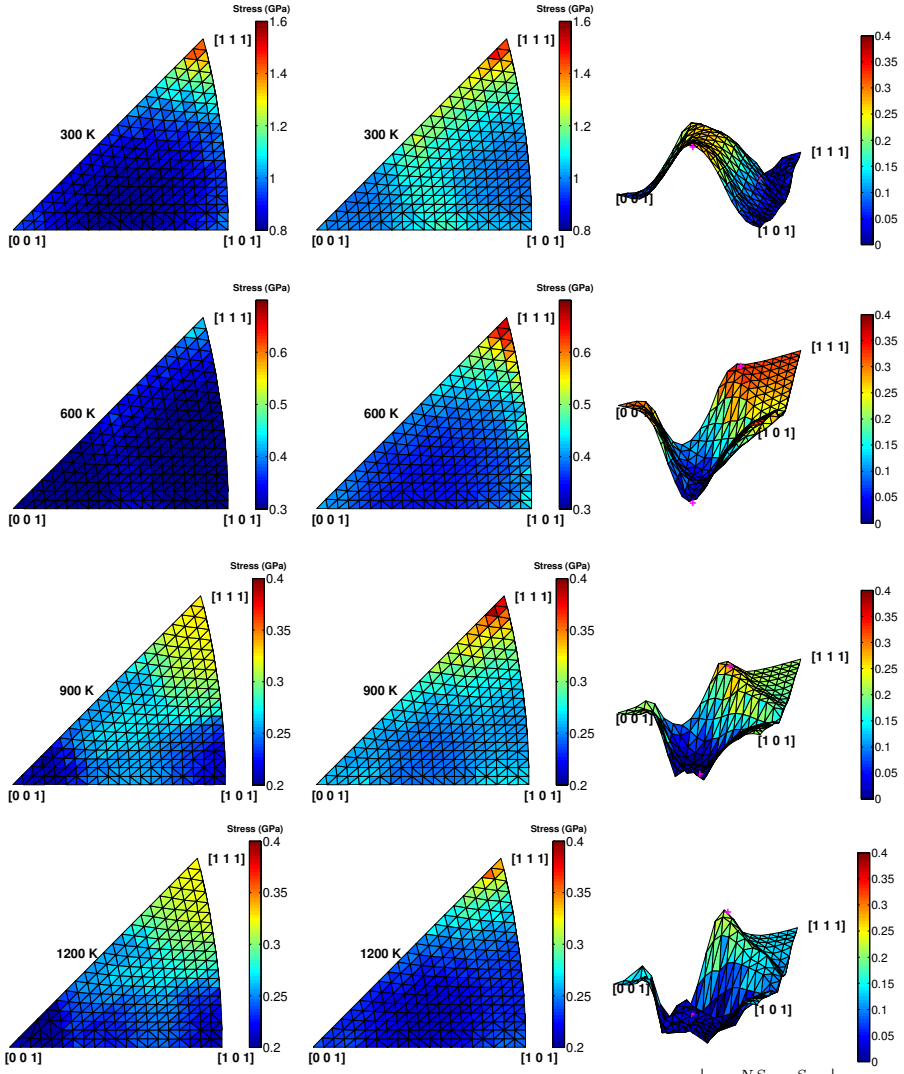

(a) Schmid (b) non-Schmid (c) $\left|\frac{\sigma_y^{NS}-\sigma_y^{S}}{(\sigma_y^{NS}+\sigma_y^{S})/2}\right|$

Fig. 7 (online colour at: www.gamm-mitteilungen.org) Yield strength for uniaxial tensile tests along 231 uniformly distributed crystallographic orientations in the standard triangle at different temperatures. Schmid and non-Schmid behaviors are studied separately. $\{1\,1\,0\}\langle 1\,1\,1\rangle$ and $\{1\,1\,2\}\langle 1\,1\,1\rangle$ slip systems are active. Fig. 7(c) represents the difference relative to unity between non-Schmid and Schmid.

shown in Fig. 5 confirm the low impact of activating additional $\{1\,1\,2\}$ planes even when they are considered active during slip. These results, in agreement with previous work from Caillard [79,80], show that for the entire range of temperature studied, slip of screw dislocations takes place primarily on $\{1\,1\,0\}$ planes.

- In agreement with previous works in other bcc metals [52–54], results in Fig. 5 show that the yield strength rapidly decreases with temperature in single-crystal tungsten.
- The yield strength shown in Fig. 4, Fig. 5, and Fig. 7 clearly depends on the loading orientation of the tensile test. Among the 231 uniformly distributed crystallographic orientations studied here, we observe in Fig. 6 that the loading orientation of maximum yield is always $[1\,1\,1]$ while the loading orientation of minimum yield strength depends on the temperature.

Acknowledgments

Conversations and discussions with Claudio Zambaldi are gratefully acknowledged. This work was performed under the auspices of the U.S. Department of Energy by Lawrence Livermore National Laboratory under Contract No. DE-AC52-07NA27344. J. M. acknowledges support from DOE's Early Career Research Program. D. C. acknowledges support from the Consejo Social and the PhD program of the Universidad Politécnica de Madrid. M.D. acknowledges support from project number M 41.2.10410 in the framework of the Research Program of the Materials innovation institute (M2i) (www.m2i.nl). DC and JMP acknowledge Spanish MINECO for funding through the projects ACI2009-1040 and MAT2012-38541-C02-01 and support from the 7th Framework Programme with project HiPER: European High Power Laser Energy Research Facility, Grant Agreement No. 211737.

References

[1] S. J. Zinkle and N. M. Ghoniem, Journal of Nuclear Materials **417**(1), 2–8 (2011).
[2] M. Rieth, S. Dudarev, S. Gonzalez de Vicente, J. Aktaa, T. Ahlgren, S. Antusch, D. Armstrong, M. Balden, N. Baluc, M. F. Barthe *et al.* , Journal of Nuclear Materials **432**(1), 482–500 (2013).
[3] H. Bolt, V. Barabash, W. Krauss, J. Linke, R. Neu, S. Suzuki, N. Yoshida, and A. U. Team, Journal of nuclear materials **329**, 66–73 (2004).
[4] V. Vitek, R. Perrin, and D. Bowen, Philosophical Magazine **21**(173), 1049–1073 (1970).
[5] V. Vitek, Philosophical Magazine **84**(3-5), 415–428 (2004).
[6] S. Ismail-Beigi and T. Arias, Physical Review Letters **84**(7), 1499 (2000).
[7] W. Cai, V. V. Bulatov, J. Chang, J. Li, and S. Yip, Dislocations in solids **12**, 1–80 (2004).
[8] D. Raabe, Materials science and technology **11**(5), 455–460 (1995).
[9] A. Ma, F. Roters, and D. Raabe, Computational Materials Science **39**(1), 91 – 95 (2007), Proceedings of the 15th International Workshop on Computational Mechanics of Materials The 15th International Workshop on Computational Mechanics of Materials.
[10] B. Sestak and A. Seeger, Zeitschrift fuer Metallkunde/Materials Research and Advanced Techniques **69**(4), 195–202 (1978).
[11] J. Christian, Metallurgical Transactions A **14**(7), 1237–1256 (1983).
[12] W. Spitzig and A. Keh, Acta Metallurgica **18**(6), 611 – 622 (1970).
[13] D. Brunner, International Journal of Materials Research **101**(8), 1003–1013 (2010).
[14] R. Madec and L. Kubin, Dislocation interactions and symmetries in bcc crystals, in: IUTAM Symposium on Mesoscopic Dynamics of Fracture Process and Materials Strength, (2004), pp. 69–78.
[15] S. Van Petegem, H. Van Swygenhoven, C. Borca, C. Marichal *et al.* , Scientific Reports **3**(EPFL-ARTICLE-189315) (2013).
[16] E. Schmid and W. Boas(1950), W. Kristallplastizitt., Springer, Berlin (1935), translated in English.

[17] M. a. S. Duesbery and V. Vitek, Acta Materialia **46**(5), 1481–1492 (1998).
[18] Q. Qin and J. L. Bassani, Journal of the Mechanics and Physics of Solids **40**(4), 813 – 833 (1992).
[19] J. Rice, Journal of the Mechanics and Physics of Solids **19**(6), 433–455 (1971).
[20] J. Hutchinson, Proceedings of the Royal Society of London. A. Mathematical and Physical Sciences **348**(1652), 101–127 (1976).
[21] D. Peirce, R. Asaro, and A. Needleman, Acta metallurgica **30**(6), 1087–1119 (1982).
[22] D. Peirce, R. J. Asaro, and A. Needleman, Acta metallurgica **31**(12), 1951–1976 (1983).
[23] A. Arsenlis and D. M. Parks, Journal of the Mechanics and Physics of Solids **50**(9), 1979 – 2009 (2002).
[24] A. Arsenlis, D. M. Parks, R. Becker, and V. V. Bulatov, Journal of the Mechanics and Physics of Solids **52**(6), 1213 – 1246 (2004).
[25] A. Ma, F. Roters, and D. Raabe, Acta Materialia **54**(8), 2169 – 2179 (2006).
[26] A. Arsenlis and D. Parks, Acta Materialia **47**(5), 1597 – 1611 (1999).
[27] K. S. Cheong and E. P. Busso, Acta Materialia **52**(19), 5665 – 5675 (2004).
[28] A. Ma and F. Roters, Acta Materialia **52**(12), 3603 – 3612 (2004).
[29] A. Alankar, D. Field, and H. Zbib, Philosophical Magazine **92**(24), 3084–3100 (2012).
[30] B. Peeters, S. Kalidindi, P. Van Houtte, and E. Aernoudt, Acta materialia **48**(9), 2123–2133 (2000).
[31] L. Stainier, A. M. Cuitiño, and M. Ortiz, Journal of the Mechanics and Physics of Solids **50**(7), 1511–1545 (2002).
[32] J. Raphanel and P. Van Houtte, Acta Metallurgica **33**(8), 1481–1488 (1985).
[33] P. Erieau and C. Rey, International Journal of Plasticity **20**(10), 1763–1788 (2004).
[34] K. Kitayama, C. Tomé, E. Rauch, J. Gracio, and F. Barlat, International Journal of Plasticity **46**, 54–69 (2013).
[35] M. Hölscher, D. Raabe, and K. Lücke, Steel Research International(62), 567–575 (1991).
[36] M. Hölscher, D. Raabe, and K. Lücke, Acta metallurgica et materialia **42**(3), 879–886 (1994).
[37] D. Raabe, G. Schlenkert, H. Weisshaupt, and K. Lücke, Materials science and technology **10**(4), 299–305 (1994).
[38] D. Raabe, Materials Science and Engineering: A **197**(1), 31–37 (1995).
[39] C. Hamelin, B. Diak, and A. Pilkey, International Journal of Plasticity **27**(8), 1185–1202 (2011).
[40] A. Koester, A. Ma, and A. Hartmaier, Acta Materialia **60**(9), 3894–3901 (2012).
[41] C. R. Weinberger, C. C. Battaile, T. E. Buchheit, and E. A. Holm, International Journal of Plasticity **37**, 16–30 (2012).
[42] S. Narayanan, D. L. McDowell, and T. Zhu, Journal of the Mechanics and Physics of Solids **65**(0), 54 – 68 (2014).
[43] A. Patra, T. Zhu, and D. L. McDowell, International Journal of Plasticity **59**, 1 – 14 (2014).
[44] H. Lim, C. C. Battaile, J. D. Carroll, B. L. Boyce, and C. R. Weinberger, Journal of the Mechanics and Physics of Solids **74**, 80–96 (2015).
[45] H. Lim, L. Hale, J. Zimmerman, C. Battaile, and C. Weinberger, International Journal of Plasticity (2015).
[46] Y. J. Lee, G. Subhash, and G. Ravichandran, International Journal of Plasticity **15**(6), 625–645 (1999).
[47] S. Kuchnicki, R. Radovitzky, and A. Cuitiño, International Journal of Plasticity **24**(12), 2173–2191 (2008).
[48] H. Lim, C. R. Weinberger, C. C. Battaile, and T. E. Buchheit, Modelling and Simulation in Materials Science and Engineering **21**(4), 045015 (2013).
[49] A. Alankar, D. P. Field, and D. Raabe, International Journal of Plasticity **52**, 18 – 32 (2014), In Honor of Hussein Zbib.
[50] M. Knezevic, I. J. Beyerlein, M. L. Lovato, C. N. Tomé, A. W. Richards, and R. J. McCabe, International Journal of Plasticity **62**, 93–104 (2014).
[51] E. Lassner and W. D. Schubert, Tungsten: Properties, Chemistry, Technology of the Element, Alloys, and Chemical Compounds. (Springer US, 1999).

[52] S. Narayanan, D. L. McDowell, and T. Zhu, Journal of the Mechanics and Physics of Solids **65**, 54 – 68 (2014).
[53] E. Kuramoto, Y. Aono, and K. Kitajima, Scripta Metallurgica **13**(11), 1039–1042 (1979).
[54] D. Brunner and J. Diehl, Physica Status Solidi (A) Applied Research **124**(1), 155–170 (1991).
[55] C. Reina and S. Conti, Journal of the Mechanics and Physics of Solids **67**, 40 – 61 (2014).
[56] V. Vitek, Philosophical Magazine **84**(3-5), 415–428 (2004).
[57] J. P. C. J. L. W. CaiV.V. Bulatov. and S. Yip, Dislocation core effects on mobility in: Dislocation in Solids (Elsevier, 2002).
[58] A. Hartmaier and P. Gumbsch, Phys. Rev. B **71**(Jan), 024108 (2005).
[59] D. L. Olmsted, L. G. H. Jr, W. A. Curtin, and R. J. Clifton, Modelling and Simulation in Materials Science and Engineering **13**(3), 371 (2005).
[60] M. R. Gilbert, S. Queyreau, and J. Marian, Phys. Rev. B **84**(Nov), 174103 (2011).
[61] D. Cereceda, A. Stukowski, M. R. Gilbert, S. Queyreau, L. Ventelon, M. C. Marinica, J. M. Perlado, and J. Marian, Journal of Physics: Condensed Matter **25**(8), 085702 (2013).
[62] K. Lin and D. C. Chrzan, Phys. Rev. B **60**(Aug), 3799–3805 (1999).
[63] C. S. Deo, D. J. Srolovitz, W. Cai, and V. V. Bulatov, Phys. Rev. B **71**(Jan), 014106 (2005).
[64] A. Stukowski, D. Cereceda, T. D. Swinburne, and J. Marian, International Journal of Plasticity **65**, 108–130 (2015).
[65] S. Queyreau, G. Monnet, and B. Devincre, International Journal of Plasticity **25**(2), 361 – 377 (2009).
[66] A. Ma, F. Roters, and D. Raabe, Computational Materials Science **39**(1), 91 – 95 (2007), Proceedings of the 15th International Workshop on Computational Mechanics of Materials The 15th International Workshop on Computational Mechanics of Materials.
[67] F. Roters, P. Eisenlohr, L. Hantcherli, D. Tjahjanto, T. Bieler, and D. Raabe, Acta Materialia **58**(4), 1152 – 1211 (2010).
[68] F. Roters, Advanced material models for the crystal plasticity finite element method: development of a general CPFEM framework (Universitätsbibliothek, 2011).
[69] F. Roters, P. Eisenlohr, C. Kords, D. Tjahjanto, M. Diehl, and D. Raabe, Procedia IUTAM **3**, 3 – 10 (2012), IUTAM Symposium on Linking Scales in Computations: From Microstructure to Macro-scale Properties.
[70] P. Eisenlohr, M. Diehl, R. Lebensohn, and F. Roters, International Journal of Plasticity **46**, 37 – 53 (2013), Microstructure-based Models of Plastic Deformation.
[71] P. Shanthraj, P. Eisenlohr, M. Diehl, and F. Roters, International Journal of Plasticity **66**, 31 – 45 (2015), doi:10.1016/j.ijplas.2014.02.006
[72] C. Kords and D. Raabe, On the role of dislocation transport in the constitutive description of crystal plasticty, PhD thesis, Berlin, 2013.
[73] D. Cereceda, A. Stukowski, M. Gilbert, S. Queyreau, L. Ventelon, M. Marinica, J. Perlado, and J. Marian, Journal of Physics: Condensed Matter **25**(8), 085702 (2013).
[74] M. C. Marinica, L. Ventelon, M. R. Gilbert, L. Proville, S. L. Dudarev, J. Marian, G. Bencteux, and F. Willaime, Journal of Physics: Condensed Matter **25**(39), 395502 (2013).
[75] P. Franciosi, L. Le, G. Monnet, C. Kahloun, and M. H. Chavanne, International Journal of Plasticity **65**, 226–249 (2015).
[76] D. Brunner, International Journal of Materials Research **101**(8), 1003–1013 (2010).
[77] A. S. Keh, Philosophical Magazine **12**(115), 9–30 (1965).
[78] W. Callister and D. Rethwisch, Materials Science and Engineering: An Introduction (John Wiley & Sons Canada, Limited, 2009).
[79] D. Caillard, Acta Materialia **58**(9), 3493–3503 (2010).
[80] D. Caillard, Acta Materialia **58**(9), 3504–3515 (2010).

